Chapter 3

Analytic modelling of elastic wave propagation

This chapter is devoted to analytic modelling of elastic wave propagation. The starting point is the concept of a plane wave providing important qualitative insight into wave propagation, especially in anisotropic materials. From there on, wave propagation due to a line source at the free surface of an elastic half-space is considered. This problem involves initial - and boundary conditions with the solution being constructed from plane waves. The solution to the latter problem provides valuable information about the nature of the sound field from a transducer.

3.1 Plane wave solution

A plane wave is specified[1] by

$$\boldsymbol{u}(\boldsymbol{x},t) = \alpha \boldsymbol{u}_0 \mathrm{e}^{\mathrm{i}(\omega t - \boldsymbol{k}\cdot\boldsymbol{x})} \tag{3.1}$$

where α is the amplitude of the plane wave and $\boldsymbol{u}_0$ is the *polarization vector* of unit length. $\omega = 2\pi f$ is the circular frequency and $\boldsymbol{k}$ is the wave vector. The length of the wave vector is called the wave number k with the well-known relation to the phase velocity v and wavelength λ

$$k = \frac{\omega}{v} = \frac{2\pi}{\lambda} \tag{3.2}$$

We let $\boldsymbol{n}$ denote the normalized wave vector, $\boldsymbol{k} = k\boldsymbol{n}$, and define the slowness vector as $\boldsymbol{s} = \frac{1}{v}\boldsymbol{n}$. Occasionally, the term phase velocity may also refer to the vector $\boldsymbol{v} = v\boldsymbol{n}$ (that is, either a scalar or a vector). Using this notation, the plane wave may alternatively be written

$$\boldsymbol{u}(\boldsymbol{x},t) = \alpha \boldsymbol{u}_0 \mathrm{e}^{\mathrm{i}\omega(t - \boldsymbol{s}\cdot\boldsymbol{x})} \tag{3.3}$$

Consider now the definition of the following 3×3 matrix P

$$P_{ik}(\partial_{x_1}, \partial_{x_2}, \partial_{x_3}, \partial_t) \equiv c_{ijkl}\partial_{x_j}\partial_{x_l} - \delta_{ik}\rho\partial_t^2 \tag{3.4}$$

[1]As always, it is understood that either the real part or the imaginary part is considered.

The elastodynamic equations (2.11) may then be written in matrix form

$$\boldsymbol{P}(\partial_{x_1}, \partial_{x_2}, \partial_{x_3}, \partial_t)\boldsymbol{u} = -\rho \boldsymbol{f} \tag{3.5}$$

We shall in the remaining part of this chapter consider the homogeneous problem, $\boldsymbol{f} = \boldsymbol{0}$. Insertion of (3.1) into the (3.5) provides us with the following condition, called the *Christoffel equation*, for the plane wave to be a solution

$$\boldsymbol{P}(\boldsymbol{k}, \omega)\boldsymbol{u}_0 = \boldsymbol{0} \tag{3.6}$$

The first matrix appearing in $\boldsymbol{P}(\boldsymbol{k}, \omega)$ is known as the 3×3 Christoffel matrix, $\Gamma_{ik} = c_{ijkl}k_j k_l$. In order for (3.6) to have non-trivial solutions $\boldsymbol{u}_0$, the matrix $\boldsymbol{P}$ should be singular

$$\Omega(\boldsymbol{k}, \omega) \equiv \det \boldsymbol{P}(\boldsymbol{k}, \omega) = 0 \tag{3.7}$$

This condition is known as the *dispersion relation*, relating the wave vector to the circular frequency, $\boldsymbol{k} = \boldsymbol{k}(\omega)$. It follows from the positive definite property of $\boldsymbol{c}$ (2.16), that for real $\boldsymbol{k}$, (3.7) has three positive real-valued roots for ω^2. Rather than working with the wave vector $\boldsymbol{k}$, it is usually more convenient to work with either $\boldsymbol{n}$ or $\boldsymbol{s}$ as they are independent of the circular frequency ω. For this purpose, the relation (3.2) may be used to express the dispersion relation (3.7) in the following two equivalent ways

$$\Omega(\boldsymbol{n}, v) \equiv \det \boldsymbol{P}(\boldsymbol{n}, v) = 0 \tag{3.8}$$
$$\Omega(\boldsymbol{s}, 1) \equiv \det \boldsymbol{P}(\boldsymbol{s}, 1) = 0 \tag{3.9}$$

(3.9) may also be obtained directly by inserting the alternative expression for the plane wave (3.3) into (3.5). From the positive definiteness noted above, it follows that there are three positive solutions (eigenvalues) $\lambda_i(\boldsymbol{n}) = \rho v^2$ to (3.8) for a given direction $\boldsymbol{n}$. This results in three phase velocities

$$v_i(\boldsymbol{n}) = \sqrt{\lambda_i(\boldsymbol{n})/\rho} \tag{3.10}$$

where the directional dependence has been emphasized. The corresponding eigenvectors are the polarization vectors $\boldsymbol{u}_0$ which are the solutions to (3.6). Due to the symmetry of the Christoffel matrix, eigenvectors corresponding to different eigenvalues are perpendicular. Geometrically, (3.8) defines the *velocity surface* consisting in general of three sheets (branches). The length of each radius vector defining a sheet is equal to the corresponding phase velocity in that direction. (3.9) defines the important *slowness surface* or *normal surface*, where the radius vector has a length equal to the inverse phase velocity. Thus, the velocity surface and the slowness surfaces are each other's inverse.

Before proceeding further it is instructive to consider the isotropic and the transversely isotropic cases in detail as they will appear often in the thesis. In the isotropic case, it is readily derived, that the three eigenvalues are independent[2] of $\boldsymbol{n}$ and that two of them coincide, $\lambda_1 = c_{11}$ and $\lambda_2 = \lambda_3 = c_{44}$. The polarization vector $\boldsymbol{u}_0$ corresponding to $\lambda_1 = c_{11}$ is easily seen to be parallel to $\boldsymbol{n}$. Consequently, the two polarization vectors corresponding to the other eigenvalue c_{44} may be chosen arbitrarily in the plane normal to $\boldsymbol{n}$. The first wave travelling with speed $v_l = \sqrt{c_{11}/\rho}$ is called the longitudinal (L)

[2]thus per definition the term *isotropic*.

or pressure (P) wave. The other wave travelling with speed $v_t = \sqrt{c_{44}/\rho}$ is called the transverse (T) or shear (S) wave[3]. Thus, in the isotropic case the velocity surface and slowness surface consist of only two sheets of spherical shape. In relation to the discussion in section 2.5.4 two types of transverse waves occur frequently within ultrasonic NDT, the shear horizontal (SH) wave and the shear vertical (SV) wave. With reference to Fig. 2.2 on p. 15, the SV wave is polarized in the vertical x_1x_3-plane (as is the longitudinal wave), while the SH wave is polarized along the (horizontal) $\boldsymbol{e}_2$ axis. For an anisotropic material, the polarization vectors will in general neither be parallel nor perpendicular to the wave vector. It is however customary to label the waves quasi-longitudinal (qL) or quasi-transverse (qT) according to their closest relationship with either a purely longitudinal or transverse wave. For transversely isotropic materials it may readily be shown by proceeding as above, that one of the waves is a pure transverse wave and furthermore that the corresponding polarization vector is perpendicular to the crystal symmetry axis. Despite this isotropic behaviour the phase velocity of this wave (as well as for the two others) is nevertheless direction dependent. We shall be concerned with a crystal axis in the x_1x_3-plane, in which case it is customary to talk about a SH, a qSV and a qL wave as a natural extension of the above terminology and referenced figure.

In a material, associated with a plane wave propagation (and it's wave vector) are the energy density and the energy flux vectors, the latter expressing the amount and direction of energy flow per unit time through a unit area perpendicular to the vector. The ratio of the time averaged energy flux vector to the time averaged energy density defines the important concept of the energy velocity or ray vector $\boldsymbol{v}_e$. For a lossless medium, which we consider in this thesis, it may be shown that this vector is equal to the group velocity $\boldsymbol{v}_g$, $\boldsymbol{v}_e = \boldsymbol{v}_g$ [7, 22] (note that in [22] the group velocity is denoted by $\boldsymbol{s}$, which is used to denote the slowness vector in this thesis). The group velocity is calculated in the standard way

$$\boldsymbol{v}_g = \frac{\partial \omega}{\partial \boldsymbol{k}} = -\frac{\nabla_{\boldsymbol{k}}\Omega(\boldsymbol{k},\omega)}{\Omega'_{\omega}(\boldsymbol{k},\omega)} = \frac{\partial v}{\partial \boldsymbol{n}} = -\frac{\nabla_{\boldsymbol{n}}\Omega(\boldsymbol{n},v)}{\Omega'_{v}(\boldsymbol{n},v)} \tag{3.11}$$

The two expressions involving Ω follow from the use of implicit differentiation of (3.7) and (3.8). These expressions may be used instead, when it is cumbersome[4] to obtain the relation $\omega = \omega(\boldsymbol{k})$. Note, that a group velocity is associated with each of the three roots v of (3.8).

The slowness surface defined above may conveniently be used to determine the direction of the energy vector(s) for a given direction of the wave vector. It may be shown [7], that at a given point $\boldsymbol{s}$ on a sheet of the slowness surface, the associated energy vector is perpendicular to the tangent vector of the sheet in that point. For isotropic materials, the slowness surfaces are spheres (circles in 2D) due to the direction independence, so we have immediately that the wave vector and the energy vector are parallel. This is, however, usually not the case for anisotropic materials, where both the direction and length may differ as the slowness surfaces are not spheres. In fact, the (length of the) group velocity is

[3] From the positive definiteness of the elastic matrix (2.16) it follows that $0 < c_{44} < \frac{3}{4}c_{11}$ and therefore $v_t < \sqrt{\frac{3}{4}}v_l$, i. e. the longitudinal wave always travels with the higher speed of the two wave types.

[4] It is the author's experience from the crystal systems considered, that expressions for $\omega = \omega(\boldsymbol{k})$ and $v = v(\boldsymbol{n})$ although at times extremely lengthy may be obtained directly from (3.7) and (3.8) respectively using an analytic tool such as Mathematica [75].

always equal to or larger than the phase velocity, as the following relationship [22] shows

$$\boldsymbol{v}_g \cdot \boldsymbol{n} = v \tag{3.12}$$

Since the group velocity and the phase velocity are parallel in isotropic materials, we immediately have from (3.12) that their lengths must be equal.

For anisotropic materials, due to the difference between the two vectors, we interpret the plane wave as propagating in the direction of the energy vector rather than in the direction of the wave vector. This is the basic idea in many ray tracing algorithms dealing with anisotropic materials. The phenomenon of the plane wave propagating at an angle to the wave vector in anisotropic materials is known as *beam skewing*.

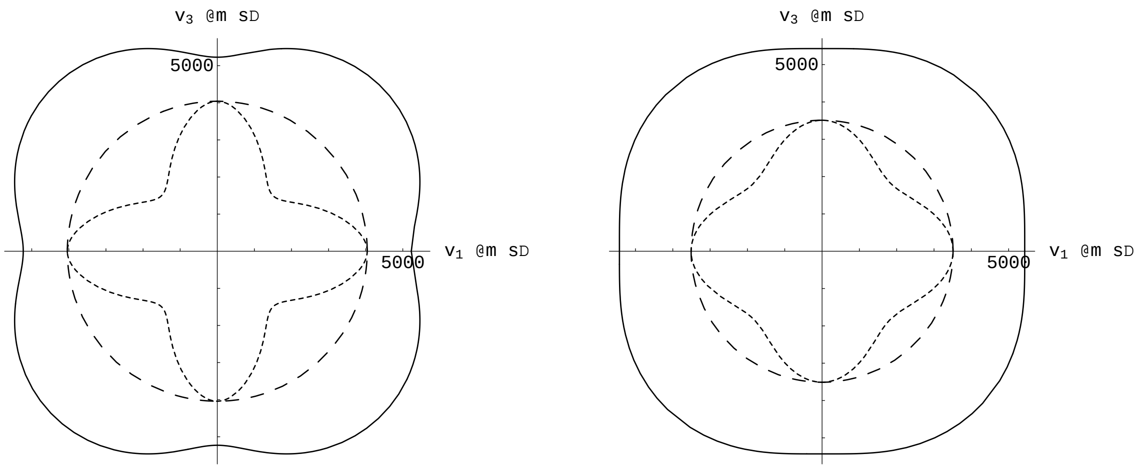

Figure 3.1: Velocity surfaces for the cubic materials X 6 CrNi 18 12 (left) and Inconel 182 (right). Full line: qL wave, dashed line: SH wave, dotted line: qSV.

The remaining part of the subsection is devoted to illustrating the concepts introduced above for anisotropic materials. As a first illustration, the velocity surfaces clearly elucidate the difference between anisotropic and isotropic materials. Since the velocity surfaces for the latter are spheres (3D) or circles (2D) with radii equal to the phase velocities, they are not shown here.

Single-crystal cubic materials will not be important in this thesis, but since they form the building block of the materials considered later, they will be given some attention at this point. The velocity surface corresponding to the three different wave types (qL, SH, qSV) in the x_1x_3-plane for cubic X 6 CrNi 18 12 and Inconel 182 (see Table 2.2 on p. 21 for elastic constants) are shown in Fig. 3.1. The pure transverse SH wave with fixed phase velocity $\sqrt{c_{44}/\rho}$ shows up when the wave vector lies in one of the three coordinate planes being the faces of the unit cell in the cubic crystal system. Note, that the velocity surface would look different in other planes. Clearly, the phase velocities depend on the direction. Relative to X 6 CrNi 18 12, the velocity surface for Inconel 182 is of a more circular form due to the anisotropy factor (2.29) being closer to unity.

The velocity surfaces for the transversely isotropic materials X 6 CrNi 18 12 and Inconel 182 (see Table 2.3 on p. 23 for elastic constants) are shown in Fig. 3.2 for the x_1x_3

(meridian) plane. Since the $\boldsymbol{e}_3$ is an axis of symmetry, the corresponding 3D surface is obtained through one revolution around this axis. Trivially, in the (isotropic) x_1x_2-plane the velocity surface reduces to circles.

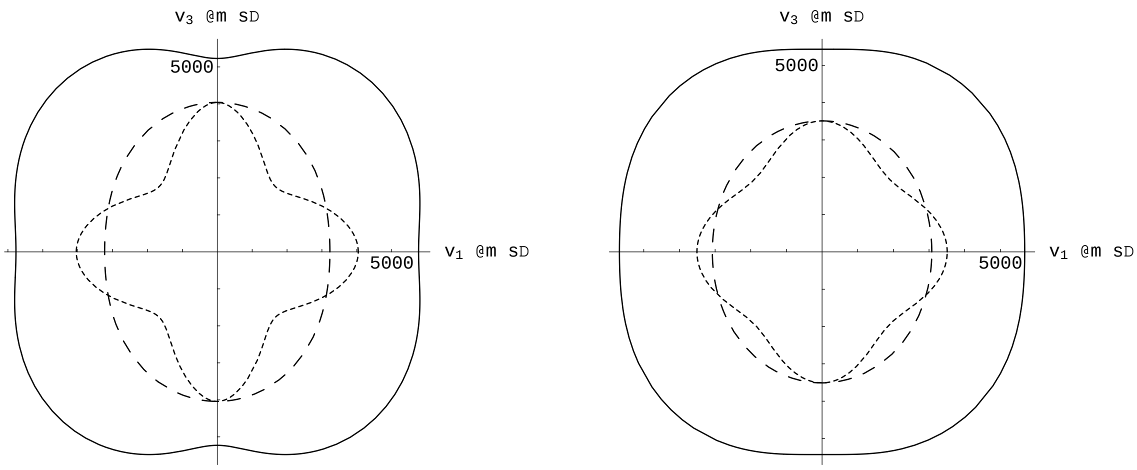

Figure 3.2: Velocity surfaces for the transversely isotropic materials X 6 CrNi 18 12 (left) and Inconel 182 (right). Full line: qL wave, dashed line: SH wave, dotted line: qSV.

Fig. 3.3 illustrates the important concepts of the slowness surface as well as the ray surface for the transversely isotropic material X 6 CrNi 18 12. In the left figure showing the slowness surface, it is clearly seen how the sign of the curvature of the qSV slowness curve changes several times during a rotation. A point on the surface where the sign of the curvature changes sign is known as an *inflexion point*. These play an important part in the classification of transversely isotropic materials within the area of analytic modelling [62]. As mentioned earlier, for a given direction of the wave vector, the slowness surface may be used to determine the corresponding directions of the (in general three different) energy vectors $\boldsymbol{v}_g$, one for each wave mode, as mentioned earlier. In the figure, this construction of the direction of the energy vector for the qSV wave is shown. Also illustrated is the relation (3.12). The right figure shows the ray surface. Note the four cuspidal triangles on the qSV curve. These are called *lacunas* and are a result of the existence of inflexion points on the corresponding slowness curve. The wave fields inside these (moving) lacunas are identically zero [62]. This is illustrated later in plots of the solution to the line source problem. Also illustrated in the figure is the method of construction of the directions and lengths of the wave vectors corresponding to a given energy vector. In the figure, this is shown for the qSV wave, but it is clearly seen that in fact five different wave vectors (three of qSV mode) may be constructed. Thus five waves with *different* wave vectors may be travelling in the same direction (although with different speeds) given by this energy vector. In this example, the existence of three qSV mode waves is a result of the inflexion points on the corresponding slowness surface. Since the 3D slowness surface is obtained through one revolution of the slowness surface in Fig. 3.3 around the crystal symmetry axis (here the x_3 axis), it follows that the energy vectors lie in the plane defined by the symmetry axis and the wave vector.

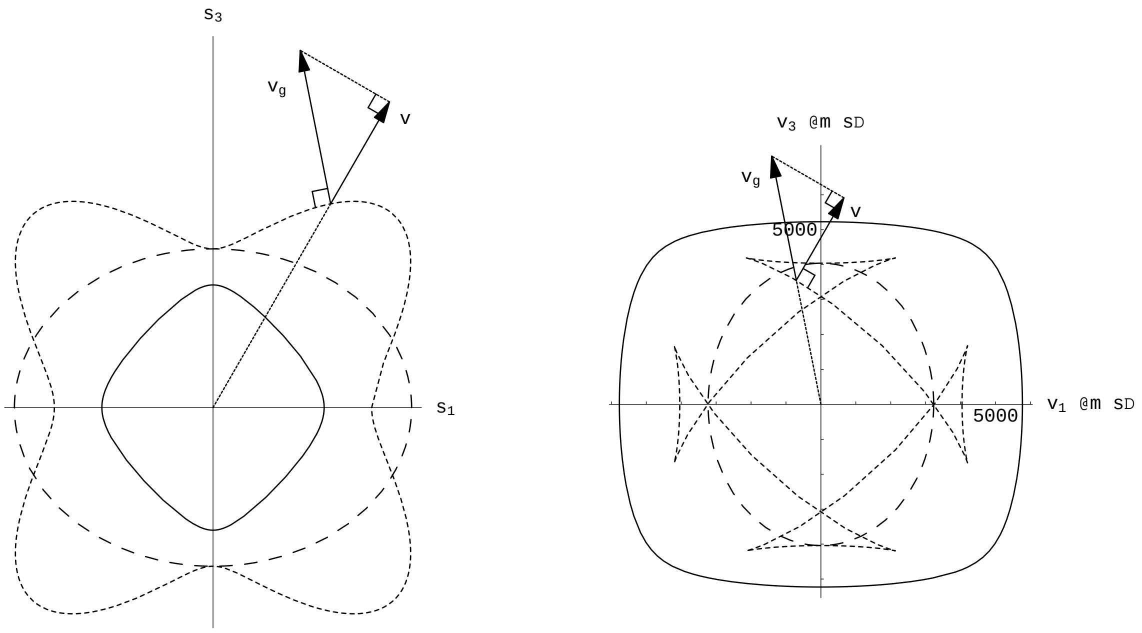

Figure 3.3: Slowness surface (left) and ray surface (right) for the transversely isotropic material X 6 CrNi 18 12. Full line: qL wave, dashed line: SH wave, dotted line: qSV.

The phenomenon of beam skewing is illustrated in Fig. 3.4 for the transversely isotropic materials X 6 CrNi 18 12 (left) and Inconel 182 (right). The figure shows the angle Δ between the wave vector and the energy vector as a function of the angle θ between the wave vector and the symmetry axis for the three different wave modes. It is seen, that for some angles $\theta = 0°, 90°$ there is no beam skewing at all, i. e. the energy vector and the wave vector are parallel for all three waves. At $\theta = 43.2°$, the qSV experiences no beam skewing, while the two other wave types do. At $\theta = 49.1°$ this situation is true instead for the qL wave. While the two plots in the figure are of the same form, the beam skewing is much more pronounced in the austenitic case (about a factor two).

As a final illustration of the importance of slowness surfaces, the problem of reflection and refraction at an interface between two different materials is considered. At an interface, continuity of displacement vector and traction vector is normally required [7], resulting in six equations

$$\boldsymbol{u}_{(1)} = \boldsymbol{u}_{(2)} \tag{3.13a}$$

$$\boldsymbol{\sigma}_{(1)} \cdot \boldsymbol{n} = \boldsymbol{\sigma}_{(2)} \cdot \boldsymbol{n} \tag{3.13b}$$

The subscripts (1) and (2) refer to the two different materials and $\boldsymbol{n}$ denotes a normal vector to the interface. Using Hooke's law (2.9), the second equation involves the displacement vector as well. Considering plane waves at a plane interface, the well-known Snell's law

$$\frac{\sin(\theta_{inc})}{v_{inc}} = \frac{\sin(\theta_{ref})}{v_{ref}} \tag{3.14}$$

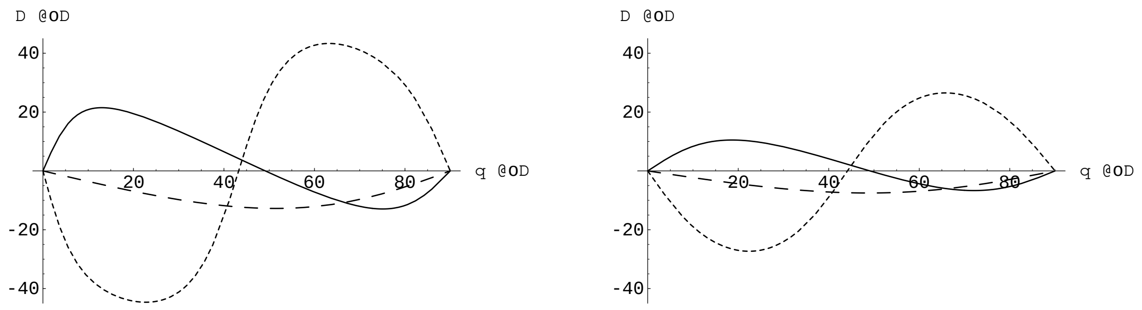

Figure 3.4: Beam skewing for the transversely isotropic materials X 6 CrNi 18 (left) 12 and Inconel 182 (right). Δ is the angle from the wave vector to the energy vector, θ is the angle from the symmetry axis to the wave vector. In both cases anti-clockwise is positive. Full line: qL wave, dashed line: SH wave, dotted line: qSV.

relating the directions of the incident wave and the reflected/refracted wave is a necessary condition for the phases of the plane waves (3.1) to be equal along the interface at all times. As the inverse of the velocities appear in Snell's law (3.14), the direction of the generated wave vectors may easily be constructed geometrically using the slowness surfaces of the involved materials. Once the wave vectors and the corresponding polarization vectors have been determined, the above six equations may then be used to determine the unknown amplitudes of the in general six involved waves (three reflected and three refracted). For anisotropic materials, this must usually be performed numerically.

This geometric approach is illustrated in Fig. 3.5 (left) for an incident transverse wave (thick vector) with an angle of incidence equal to 20° and an interface between two isotropic materials. The vertical line is drawn through the intersection between this vector and it's slowness surface. The intersections between this line and the other slowness surfaces define wave vector directions satisfying Snell's law (here two reflected and two refracted waves). The two sets of slowness surfaces (coordinate systems) should actually be placed at the interface in the point considered (isotropy/anisotropy is a point property), but for reasons of clarity they have been pulled apart.

When considering anisotropic materials, the ability to construct the energy vector directly from the slowness surface comes in very handy, since we interpret the plane wave as propagating along the energy vector rather than along the wave vector. It is assumed that only those waves whose wave vectors satisfying Snell's law and whose energy vectors point into the right material are generated. This is illustrated in Fig. 3.5 (right) for an interface between an isotropic material and an anisotropic material and with an incident transverse wave (thick vector) with an angle of incidence equal to 70°. There is one reflected transverse wave and three refracted waves (two qSV waves and one SH wave). The dotted energy vectors in the anisotropic material represent waves that are not generated as these point into the other material. Note, that the refracted qSV1 wave has a wave vector pointing into the other material, but with the energy vector pointing in the right direction. This serves to illustrate how non-intuitive wave propagation in anisotropic materials may be. It should be emphasized, that although the geometric solution just illustrated is fast and easy, the involved equations (3.14) and (3.13) should of course be solved numerically or analytically in order to obtain the exact solution.

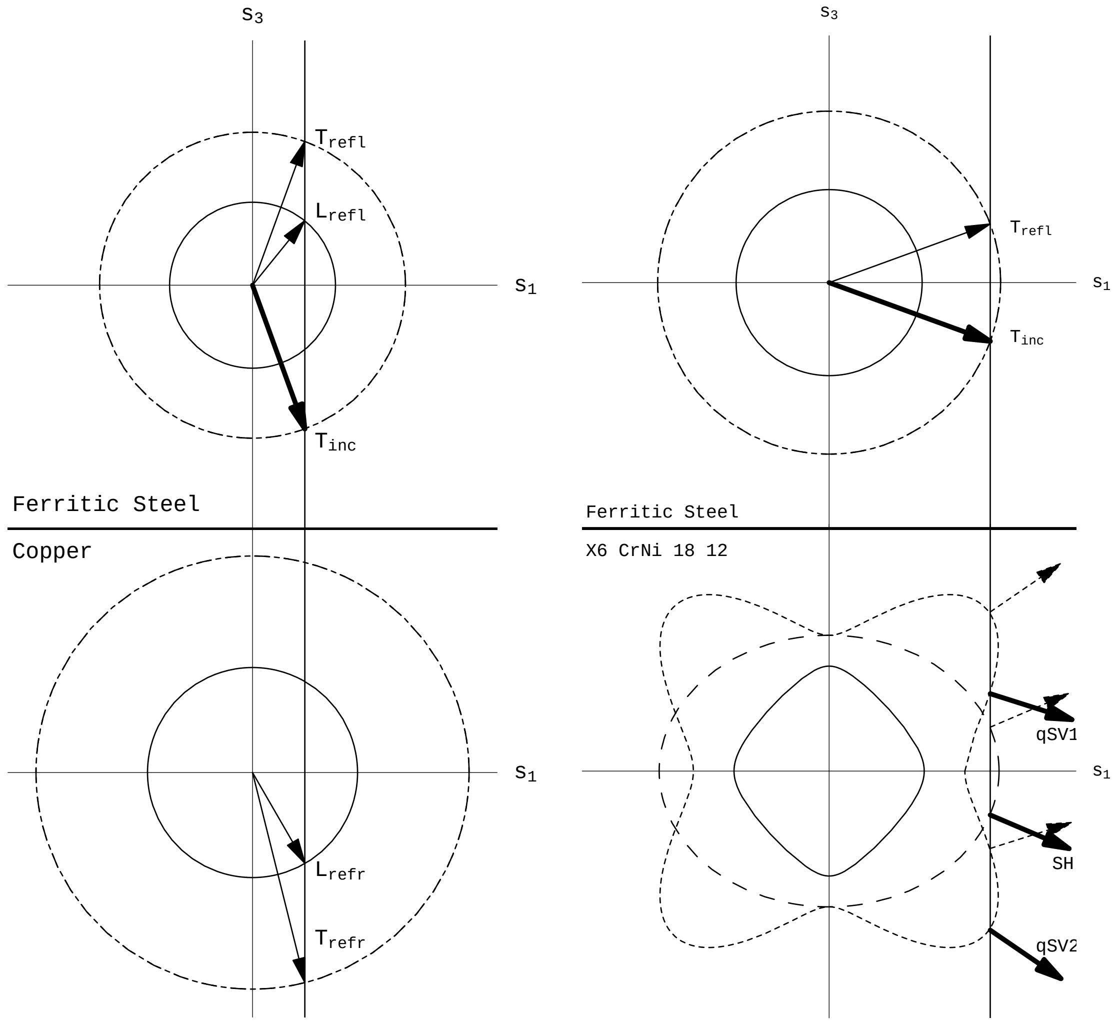

Figure 3.5: Geometrical construction of the wave vector direction for the generated waves at an interface between two materials. Left: Interface between two isotropic materials. In the upper material, the incident wave (thick vector) is a transverse wave with angle of incidence equal to 20°. Right: Interface between an isotropic material (upper) and an anisotropic material (lower). From the isotropic (upper) side the incident wave (thick vector) is a transverse wave with an angle of incidence equal to 70°. Lengths of the energy vectors (lower) are not representative.

For the sake of completeness, the phenomenon of the critical angle is mentioned. The critical angle of an incident wave occurs when the wave vector of a reflected or refracted wave becomes parallel to the interface (for an isotropic material), in which case an evanescent wave is generated. Such a wave decays exponentially away from the surface and carries no energy. At such an angle there is a drastic jump in the amplitudes of the other generated waves. This can be taken advantage of experimentally when measuring velocities. In the case of anisotropic materials, the critical angle occurs when the energy vector of one of the generated waves becomes parallel to the interface instead. Obviously, there may be several critical angles for an incident wave. These critical angles may also be illustrated using the slowness surface. For more information on this see [8, 30].

3.2 Line force on the free surface of an anisotropic medium

Plane waves as solutions to the elastodynamic equations together with important concepts such as the slowness surface were studied in the last section. In this section the elastodynamic field from a source at the free surface of a homogeneous anisotropic medium is calculated. The free surface imposes boundary conditions which a single plane wave doesn't satisfy. A solution must therefore be constructed from a superposition of plane waves. The solution to this problem is important in ultrasonic NDT because it allows the true sound field from a transducer on a scanning surface to be modelled. Furthermore, the analytic solution provides a valuable tool for validating the numerical approach described later. As suggested in the last section such a sound field in an anisotropic medium is far from being trivial.

The basic problem of a (normal) line load or point load at the free surface of an elastic medium (Lamb's problem) has a long history, which may serve to illustrate part of the development of analytic modelling within this area. A solution to the problem for an isotropic medium was first formulated by Lamb in 1904 in his classical paper [41]. The solution was based on Fourier transforms in space and time and for time-harmonic excitations the integrals could be evaluated only in the far-field using the method of stationary phase or steepest descend. In 1938 Cagniard [17, 18] constructed a suitable distortion of the integration contour leading to an exact closed expression for the displacement as a function of time. In 1960 de Hoop [36] simplified the approach by Cagniard leading to a relatively simple procedure which today is known as the Cagniard–de Hoop method. The solution was however still restricted to isotropic media. In 1960 Kraut [39] extended the Cagniard–de Hoop method to transversely isotropic media for special cases. A crucial step was made by Burridge in 1970 [15] who by studying the slowness surface and applying the Cagniard–de Hoop method was able to solve the problem for the most general anisotropy class [16].

As opposed to a construction of the solution in the Fourier domain, an approach followed in some of the methods mentioned in section 2.6, the recent approach in [72] which is reviewed and applied here formulates a direct construction of the Green's function in space and time domain. The general solution is then found using convolutions in time and space.

First, the 2D Green's problem is formulated with reference to Fig. 3.6. The anisotropic medium occupies the half-space $x_3 > 0$ and is assumed to be at rest at times $t < 0$. The free surface imposes the boundary condition $\sigma_{i3} = 0$ at $x_3 = 0$. A line source is placed along the $\boldsymbol{e}_2$ axis at $x_1 = 0$ on the surface and acting in the direction $\boldsymbol{q}$. A time dependence $\delta(t)$ excites the medium. The Green's function being the solution to this problem is denoted $\boldsymbol{g}(x_1, x_3, t)$.

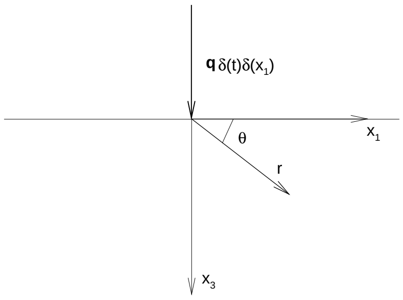

Figure 3.6: Illustration of Lamb's problem.

Introducing the boundary condition matrix $\boldsymbol{C}(\partial_{x_1}, 0, \partial_{x_3})$ using Hooke's law (2.9)

$$C_{ik}(\partial_{x_1}, 0, \partial_{x_3}) \equiv c_{i3kl}\partial_{x_l}$$

we obtain the problem statement

$$\begin{aligned} \boldsymbol{P}(\partial_{x_1}, 0, \partial_{x_3}, \partial_t)\boldsymbol{g} &= \mathbf{0}, & x_3 > 0 \quad (3.15)\\ \boldsymbol{C}(\partial_{x_1}, 0, \partial_{x_3})\boldsymbol{g} &= -\boldsymbol{q}\delta(x_1)\delta(t), & x_3 = 0 \quad (3.16)\\ \boldsymbol{g} &= \mathbf{0}, & t < 0 \quad (3.17) \end{aligned}$$

in accordance with (2.13). A solution is constructed from a superposition of plane waves on the form (compare with (3.3))

$$\alpha \boldsymbol{u}_0 f(t - s_1 x_1 - s_3 x_3) \tag{3.18}$$

with notation as in (3.3) and f being an arbitrary function at this point. This expression inserted into (3.15) results in the previously introduced Christoffel equation (3.6)

$$\boldsymbol{P}(s_1, 0, s_3, 1)\boldsymbol{u}_0 = \mathbf{0} \tag{3.19}$$

and the equation for the slowness surface (3.9)

$$\det \boldsymbol{P}(s_1, 0, s_3, 1) = 0 \tag{3.20}$$

(3.20) defines the roots of a sextic polynomium determining six (complex) functions $s_3^N(s_1)$, $N = 1, \ldots, 6$. Thus, for a given s_1 we have six plane waves on the form (3.18). The solution, however, only utilizes three of these, to be determined later by the initial condition (3.17). Consider now a solution on the form

$$\boldsymbol{g} = \mathrm{Re} \int_{-\infty}^{\infty} \sum_{N=1}^{3} \alpha^N \boldsymbol{u}_0^N f(t - s_1 x_1 - s_3^N(s_1) x_3)\, \mathrm{d}s_1 \tag{3.21}$$

Assume for the moment that $\boldsymbol{u}_0^N$ satisfies the Christoffel equation (3.19). Then obviously, (3.21) also satisfies (3.19). α^N and f must now be constructed such that the boundary condition (3.16) is satisfied. Inserting (3.21) into (3.16) shows that these are satisfied provided that

$$\sum_{N=1}^{3} \boldsymbol{C}(s_1, 0, s_3^N)\boldsymbol{u}_0^N \alpha^N = \boldsymbol{q} \tag{3.22}$$

and

$$\int_{-\infty}^{\infty} f'(t - s_1 x_1)\,\mathrm{d}s_1 = \delta(x_1)\delta(t) \tag{3.23}$$

The separation into time-independent and time-dependent conditions is fundamental to this approach. Using the adjoint matrix[5] Adj $\boldsymbol{P}$ to a quadratic matrix $\boldsymbol{P}$, set

$$\alpha^N \boldsymbol{u}_0^N = \mathrm{Adj}\,\boldsymbol{P}(\boldsymbol{s}^N, 1)\boldsymbol{T}^{-1}(s_1)\boldsymbol{q}, \qquad \boldsymbol{s}^N = (s_1, 0, s_3^N(s_1)) \tag{3.24}$$

with

$$\boldsymbol{T}(s_1) = \sum_{N=1}^{3} \boldsymbol{C}(\boldsymbol{s}^N)\mathrm{Adj}\,\boldsymbol{P}(\boldsymbol{s}^N, 1)$$

Using the property

$$\mathrm{Adj}\,\boldsymbol{P} \cdot \boldsymbol{P} = \boldsymbol{P} \cdot \mathrm{Adj}\,\boldsymbol{P} = |\boldsymbol{P}|\boldsymbol{I} \tag{3.25}$$

(3.24) is immediately seen to satisfy both (3.19) and (3.22). Thus, the usual approach of solving for $\boldsymbol{u}_0^N$ from (3.19) first and then determine α^N from (3.22) is avoided. We need to determine f from the condition (3.23). Using the following identity

$$-\frac{1}{2\pi^2}\mathrm{Re}\int_{-\infty}^{\infty} \frac{\mathrm{d}s_1}{(t - s_1(x_1 - \mathrm{i}0_+))^2} = \delta(x_1)\delta(t)$$

where 0_+ indicates a small positive value, this condition is satisfied provided

$$f(t - s_1 x_1) = \frac{1}{2\pi^2}(t - s_1(x_1 - \mathrm{i}0_+))^{-1} \tag{3.26}$$

Inserting (3.26) and (3.24) into (3.21), Green's function then takes the form

$$\boldsymbol{g} = \frac{1}{2\pi^2}\mathrm{Re}\int_{-\infty}^{\infty} \left\{ \sum_{N=1}^{3} \frac{\mathrm{Adj}\,\boldsymbol{P}(\boldsymbol{s}^N, 1)\mathrm{Adj}\,\boldsymbol{T}(s_1)\boldsymbol{q}}{\det \boldsymbol{T}(s_1)(t - s_1(x_1 - \mathrm{i}0_+) - s_3^N(s_1)x_3)} \right\} \mathrm{d}s_1 \tag{3.27}$$

where (3.25) has been used to rewrite $\boldsymbol{T}^{-1}(s_1)$. The integral will be evaluated using calculus of residues in the complex s_1 plane. The problem of choosing three of the six functions $s_3^N(s_1)$ as well as the integration contour such that the initial condition is satisfied will be described below with emphasis on the application to the transversely isotropic

[5] The transposed of the matrix of cofactors (see books on linear algebra, f. ex. [44]).

material X 6 CrNi 18 12. The crystal symmetry axis is directed along the x_3-axis with the slowness surface shown in Fig. 3.7. Only the main points are included, for a fuller discussion see the original paper [72].

It should be noted, that the slowness surface in general may be of a much more asymmetric nature than the one illustrated in Fig. 3.7, with the worst (triclinic) example exhibiting only inversion symmetry through the origin. For the considered case with the symmetry axis parallel to the x_3-axis, the slowness surface is symmetric with respect to the two axes. Thus, the six sheets $s_3^N(s_1)$ may be found analytically as they come in $\pm$ pairs. In the general case, the six sheets must be found numerically using some root finding algorithm, see f. ex. [64].

The slowness surface in Fig. 3.7 (taken from Fig. 3.3) has been divided into two groups

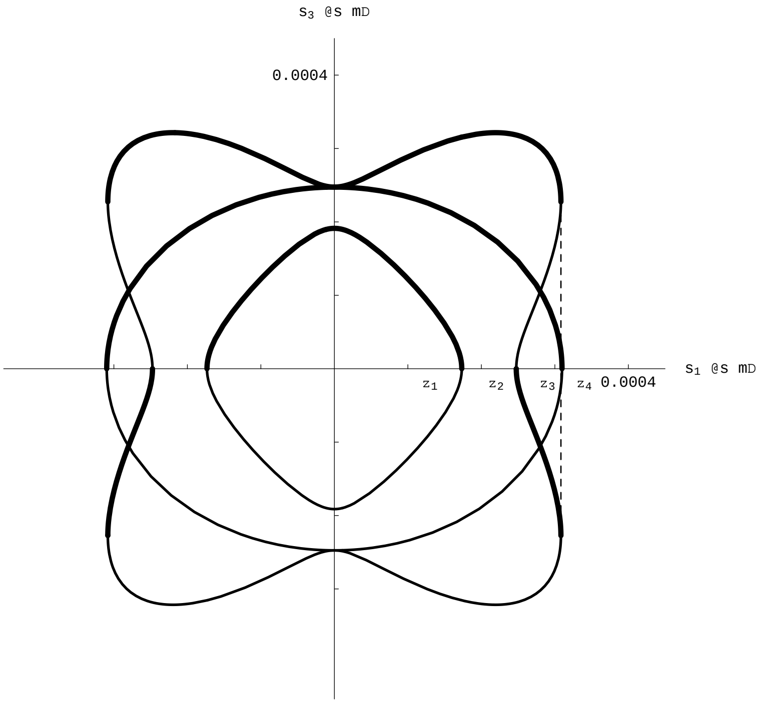

Figure 3.7: Slowness surface in the x_1x_3-plane for the transversely isotropic material X 6 CrNi 18 12 with symmetry axis along the x_3-axis.

of line segments. The first group Ξ^+ consists of those line segments (thick lines) with energy vectors pointing into the medium (positive s_3 component) while the other group Ξ^- consists of those line segments (thin lines) with energy vectors pointing out of the medium (negative s_3 component). Clearly, on each line segment the function $s_3(s_1)$ is uniquely defined. The two groups of line segments meet at the branch points $\pm\zeta_k$, $k = 1, \ldots, K$ with $0 < \zeta_1 < \ldots < \zeta_K$, and with $K = 4$ in our case (in the figure, only the positive branch points are indicated). The branch cuts, in the following denoted Ξ, are now positioned on the real s_1 axis in the interval $-\zeta_K < s_1 < \zeta_K$.

The six sheets $s_3^N(s_1)$ can be divided into two groups $s_3^N(s_1)$ and $s_3^{-N}(s_1)$ $(N = 1, 2, 3)$. The first group $s_3^N(s_1)$ yields the line segments Ξ^+ for $\mathrm{Im}\, s_1 \to 0_+$ and the line segments

Ξ^- for $\mathrm{Im}\, s_1 \to 0_-$ (in the other group $s_3^{-N}(s_1)$, the situation is reversed). The three sheets $s_3^N(s_1)$ is now chosen for the integral (3.27). This group is analytic in the complex plane except at the above positioned branch cuts. These three sheets may be identified by the property $\mathrm{Im}\,(s_3^N/s_1) < 0$ which is convenient in a programming situation.

Having found the three sheets for the integral, we finally look at the integrand. This is analytic except at the above defined branch cuts together with poles situated at $s_1 = s_1^R$ and $s_1 = s_1^N$ where

$$\det \boldsymbol{T}(s_1^R) = 0$$

and

$$t - s_1^N(x_1 - \mathrm{i}0_+) - s_3^N(s_1^N)x_3 = 0$$

respectively. Poles at $s_1 = s_1^R$ correspond to surface waves. It can be shown that these poles are real, $|s_1^R| > \zeta_K$ and that they must come in pairs $\pm s_1^R$ due to the nature of (3.20). Poles at $s_1 = s_1^N$ correspond to body waves (usual bulk waves inside the medium) and head waves (waves generated at the surface and propagating away from this). With the above choice of the three sheets $s_3^N(s_1)$ it can be shown that $\mathrm{Im}\, s_1^N > 0$ for $t > 0$ and $\mathrm{Im}\, s_1^N < 0$ for $t < 0$. With reference to Fig. 3.8, for $t > 0$ the path of integration consists of the path L along the upper side of the real s_1 axis ($\mathrm{Im}\, s_1 \to 0_+$) together with a semicircle Ω_- in the negative imaginary plane with the radius of the semicircle approaching infinity, see Fig. 3.8. The contribution along the half circle vanishes as the radius approaches infinity. Thus, according to the residue theorem, the original integral consists of a contour integral enclosing the branch cuts together with the residues of the poles at s_1^R. Using a standard evaluation of the residues of the simple poles, we have

$$\boldsymbol{g} = \mathrm{Re} \oint_{\Xi} \sum_{N=1}^{3} \left[\frac{\boldsymbol{a}^N(s_1)}{t - \lambda^N} \right] \mathrm{d}s_1 + \mathrm{Im} \sum_{N=1}^{3} \left[\frac{\boldsymbol{b}^N(s_1^R)}{t - \lambda_R^N} + \frac{\boldsymbol{b}^N(-s_1^R)}{t + \lambda_R^N} \right]$$

where

$$\begin{aligned} \boldsymbol{a}^N(s_1) &= \frac{1}{2\pi^2} \frac{\mathrm{Adj}\, \boldsymbol{P}(\boldsymbol{s}^N, 1)\mathrm{Adj}\, \boldsymbol{T}(s_1)\boldsymbol{q}}{\det \boldsymbol{T}(s_1)} \\ \boldsymbol{b}^N(s_1) &= \frac{1}{\pi} \frac{\mathrm{Adj}\, \boldsymbol{P}(\boldsymbol{s}^N, 1)\mathrm{Adj}\, \boldsymbol{T}(s_1)\boldsymbol{q}}{\partial_{s_1} \det \boldsymbol{T}(s_1)} \end{aligned}$$

and

$$\begin{aligned} \lambda^N &= s_1(x_1 - \mathrm{i}0_+) + s_3^N(s_1)x_3 \\ \lambda_R^N &= s_1^R(x_1 - \mathrm{i}0_+) + s_3^N(s_1^R)x_3 \end{aligned}$$

Using the obvious properties $s_3^N(-s_1) = -s_3^N(s_1)$, $\boldsymbol{a}^N(-s_1) = -\boldsymbol{a}^N(s_1)$ and $\boldsymbol{b}^N(-s_1) = -\boldsymbol{b}^N(s_1)$ the contour integral may be replaced with an integral along the upper sides of the branch cuts. The final expression for Green's function then becomes

$$\boldsymbol{g} = \left\{ \mathrm{Re} \int_{-\xi_K}^{\xi_K} \sum_{N=1}^{3} \left[\frac{\boldsymbol{a}^N(s_1)}{t + \lambda^N} + \frac{\boldsymbol{a}^N(s_1)}{t - \lambda^N} \right] \mathrm{d}s_1 + \mathrm{Im} \sum_{N=1}^{3} \left[\frac{\boldsymbol{b}^N(s_1^R)}{t + \lambda_R^N} + \frac{\boldsymbol{b}^N(s_1^R)}{t - \lambda_R^N} \right] \right\} H(t) \quad (3.28)$$

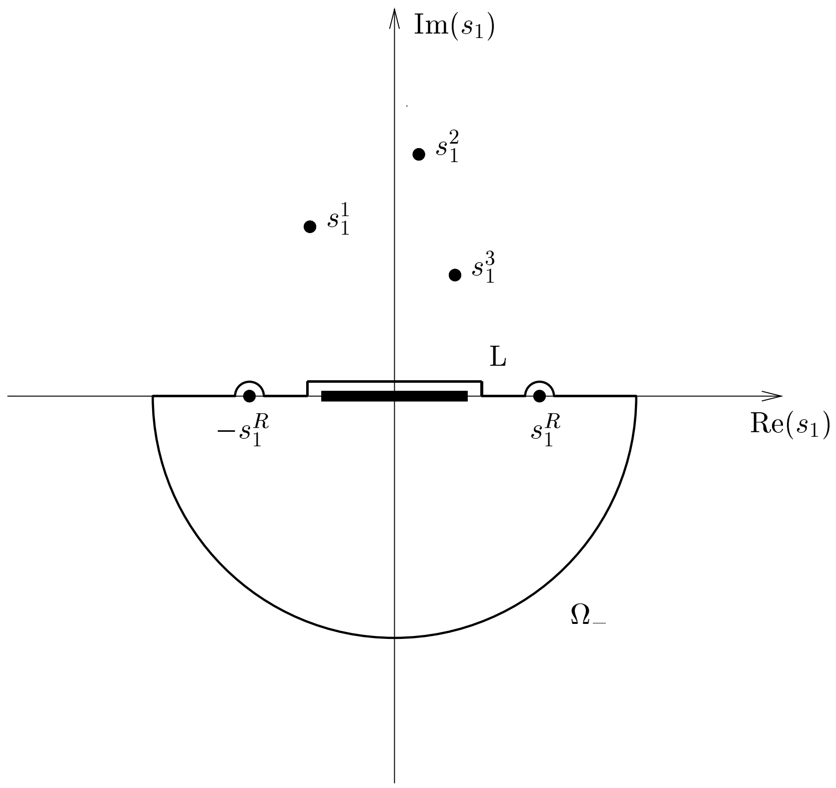

Figure 3.8: The positions of poles for $t > 0$ and the chosen integration contour in the complex s_1 plane for the integral (3.27).

A Heaviside function $H(t)$ has been added as a factor in order to emphasize the zero solution for $t < 0$. The solution $\boldsymbol{u}(x_1, x_3, t)$ for an excitation of general t and x_1 dependence $f(x_1, t)$ is obtained through a convolution with Green's function

$$\boldsymbol{u}(x_1, x_3, t) = \int_{\boldsymbol{R}^2} f(x_1 - \eta, t - \xi)\boldsymbol{g}(\eta, x_3, \xi)\, \mathrm{d}\xi\, \mathrm{d}\eta$$

Here, only an excitation with a general time dependence $f(t)$ is considered for which

$$\boldsymbol{u}(x_1, x_3, t) = \left\{ \mathrm{Re} \int_{-\xi_K}^{\xi_K} \sum_{N=1}^{3} \boldsymbol{a}^N(s_1) F(t, \lambda^N)\, \mathrm{d}s_1 + \mathrm{Im} \sum_{N=1}^{3} \boldsymbol{b}^N(s_1^R) F(t, \lambda_R^N) \right\} H(t) \quad (3.29)$$

with

$$F(t, \lambda) = \int_0^t f(t - \xi) \left(\frac{1}{\xi + \lambda} + \frac{1}{\xi - \lambda} \right) \mathrm{d}\xi \quad (3.30)$$

In the following, the numerical integration with respect to s_1 in (3.29) has been carried out using a standard integration routine from the (freely available) quadrature package QUADPACK [63].

The convolution (3.30) addresses a relevant problem. Green's function being a solution to an infinitely narrow and infinitely high pulse in time, itself exhibits localized infinite peaks as is clearly seen in the integrand. The convolution may therefore be difficult to carry out numerically, unless integration routines capable of handling such infinities are used. Solving the same problem using Fourier transformations may numerically be more attractive as the basic solution (a time-harmonic excitation with a single frequency) is more smooth. In the following, $f(t)$ has been chosen such that (3.30) could be evaluated analytically.

Before continuing with numerical examples, it is instructive to consider the boundary condition (3.16) written out in full for a transversely isotropic medium with a symmetry axis arbitrarily oriented in the x_1x_3-plane

$$\begin{pmatrix} C_{11} & 0 & C_{13} \\ 0 & C_{22} & 0 \\ C_{31} & 0 & C_{33} \end{pmatrix} \boldsymbol{u} = -\boldsymbol{q}\delta(x_1)\delta(t) \quad (3.31)$$

with C_{ij} denoting in general non-zero components. If $\boldsymbol{q} = (0, 0, 1)$ (or $\boldsymbol{q} = (1, 0, 0)$) we must have $\boldsymbol{u} = (u_1, 0, u_3)$, such that (coupled) qL waves and qSV waves will be generated. On the other hand, if $\boldsymbol{q} = (0, 1, 0)$ only a SH wave, $\boldsymbol{u} = (0, u_2, 0)$, is required in order to satisfy the boundary condition. Thus, the SH wave decouples from the two other wave types. However, in the 3D case, where the symmetry axis may be arbitrarily oriented, all three types of waves may be excited at the boundary.

Returning now to numerical examples, in [27] the time derivative of the solution (3.29) has been compared with the numerical method described in chapter 4 for a transversely isotropic medium (ice). The direction of the force is given by $\boldsymbol{q} = (0, 0, 1)$ i. e. a tensile stress. The time dependence of the excitation is given by the following polynomial expression

$$f(t) = \begin{cases} \frac{64}{a^6}(-t^6 + 3at^5 - 3a^2t^4 + a^3t^3), & 0 \leq t \leq a \\ 0, & \text{else} \end{cases} \quad (3.32)$$

where $a = T/2$ with T representing the time period. In the paper, a frequency $f = 2\,\mathrm{MHz}$ is used, giving $T = 0.5\,\mu\mathrm{s}$. The graph of the time dependence is shown in figure 3.9. Although being a model of the time dependence for a rather idealistic transducer, the

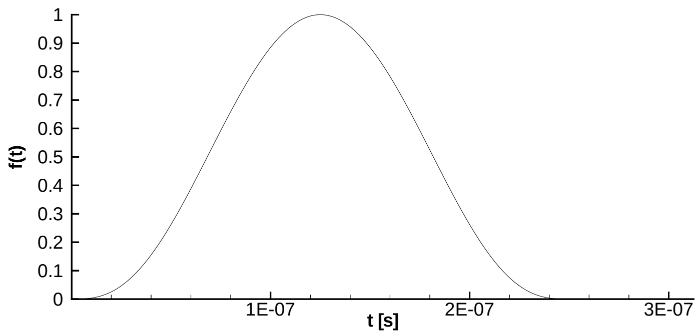

Figure 3.9: Graph of the time dependence $f(t)$ as given by (3.32).

polynomial form of (3.32) allows the convolution to be carried out analytically. The high polynomial degree ensures nice smoothness properties at the two endpoints. This is an attractive property concerning the numerical method (and thus for the comparison), as the time derivative is approximated with a finite difference.

An analytic convolution with the more realistic pulse signal $f(t;2)$ described in section 4.8 was attempted for the material X 6 CrNi 18 12. However, this resulted in a function $F(t,\lambda)$ involving sine and cosine integrals of the form $\int \sin x/x \,\mathrm{d}x$, which in principle must be evaluated numerically. A routine for evaluating these transcendental functions was written following [1,64] involving power series expansions (for small values) and continued fractions (for large values). For small distances close to the source there was an excellent agreement with the numerical solution. However, for larger distances the analytic solution started to oscillate wildly due to lack of convergence in the numerical routine for $F(t,\lambda)$. Preferably, a commercial optimized library should be used for the evaluation of the sine and cosine integrals. Thus, in the following, comparisons are shown for X 6 CrNi 18 12 using the time dependence (3.32). Due to the large numerical values of the elastic constants, it is desirable to work with scaled (dimensionless) elastic constants $\tilde{c}_{ij} = c_{ij}/c_{11}$ as well as a scaled (dimensionless) time $\tau = (t/b)\sqrt{c_{11}/\rho}$, where b simply represents unit length. In these scaled coordinates, it was found that $\zeta_4 = 1.787$ (the axes in Fig. 3.7 should be scaled with the factor $\sqrt{c_{11}/\rho} \approx 5770\,\mathrm{m/s}$ for a rough geometrical comparison) and $s_1^R = 1.949$. Thus $\zeta_4 < s_1^R$ in agreement with the previous analysis.

It should be noted, that in the computational situations reported below, it was found that especially the last term in (3.28) is rather sensitive to the choice of 0_+. After some trial and error, the choice $0_+ = 10^{-8}$ appeared to be a good choice as is evident from the figures.

The numerical method presented in chapter 4 involves the time derivative of the displacement vector i.e. the velocity vector $\boldsymbol{v} = \dot{\boldsymbol{u}}$ (not connected with the phase velocity) rather than the displacement vector itself. Thus, for the comparison below involving v_i, the time derivative of the analytic result (3.29), which basically involves (3.30), has been calculated. Fig. 3.10 shows velocity components along different radial lines emanating

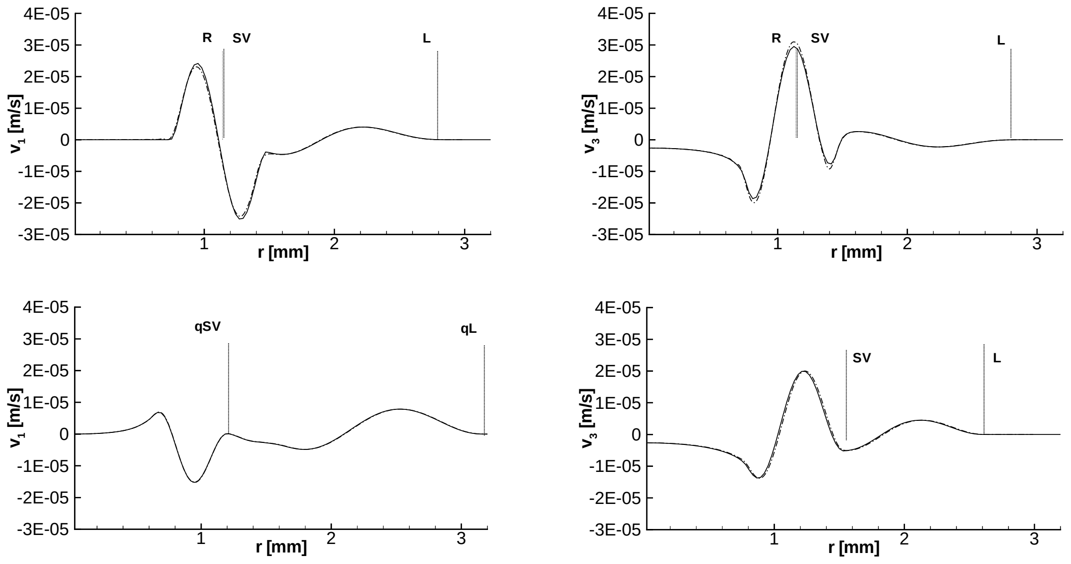

Figure 3.10: Numerical (dotted-dashed line) and analytic (solid line) solutions for v_1 and v_3 due to a line force with $\boldsymbol{q} = (0,0,1)$ at the free surface of the material X6 CrNi 18 12 as a function of the distance from the line force. The solutions are calculated at time $t = 0.5\mu$s with a time dependence as given by (3.32). The upper two plots are along the free surface $\theta = 0°$, the lower left plot is for $\theta = 45°$ and the lower right plot is for $\theta = 90°$, see Fig. 3.6. The vertical lines indicate the position of the peaks of the longitudinal, transverse and Rayleigh pulses denoted by L, SV, and R respectively as calculated from Green's function (3.28).

from the line source for the analytic and numerical solution at time $t = 0.5\,\mu$s for a normal stress $\boldsymbol{q} = (0, 0, 1)$. Also shown are the arrival times for the infinite peaks of the different wave types for the Green's function itself. The agreement between the two methods is quite good. Some discrepancy is observed at the surface around the qSV and Rayleigh wave. This may be a result of the numerical evaluation of the Rayleigh wave term in the analytic solution as mentioned above. The discrepancy does not appear to be numerical dispersion (small oscillations around the true solution) as in the case of [27]. Here it was hypothesized, that the slower speed of the Rayleigh wave resulted in the grid being too coarse. However, as the longitudinal wave is apparently not affected, the discrepancy does not appear to be some overall effect in the solutions. The large values of the Rayleigh and qSV wave compared to the longitudinal wave is clearly illustrated.

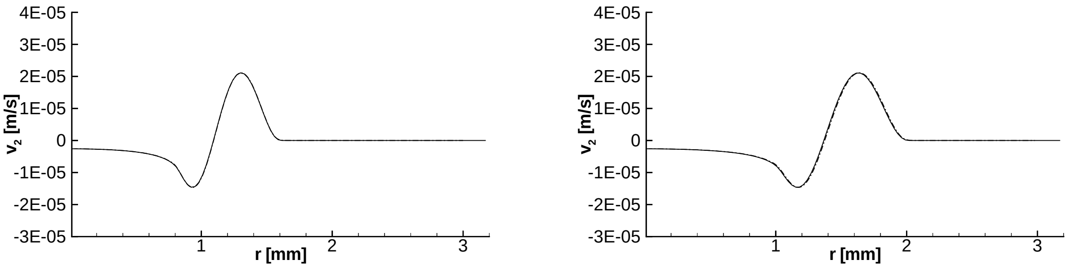

Figure 3.11: Numerical (dotted-dashed line) and analytic (solid line) solutions for v_2 for a SH excitation, $\boldsymbol{q} = (0, 1, 0)$, for $t = 0.5\,\mu$s. Left plot is along the free surface $\theta = 0°$, while the right plot is along the radial line $\theta = 90°$.

Fig. 3.11 shows the same type of plots but in the case of a shear stress $\boldsymbol{q} = (0, 1, 0)$. Only the v_2 component is observed as expected. As seen, the SH wave is not influenced by the stress free boundary, illustrating that the Rayleigh wave term in the solution is zero. Fig. 3.12 shows the contour plot for a shear stress line source $\boldsymbol{q} = (0, 1, 0)$. The SH part of the ray surface in Fig. 3.3 is clearly recognized in the plot. As before, no surface effects are observed.

Fig. 3.13 shows the much more complex contour plot in the case of a normal stress line source $\boldsymbol{q} = (0, 0, 1)$, again for $t = 0.5\,\mu$s. In the upper plot more levels are retained so that the lacunas described earlier are clearly visible. In the lower plot, a smaller number of levels are shown for ease of illustration (being the only reason for two plots). Again the ray surface for the qSV and the qL wave are recognized from Fig. 3.3. The large quasi Rayleigh waves are clearly seen at the surface. In 2D these waves are not geometrically attenuated (as opposed to the 3D case) as they travel along the surface. Thus, at large distances they will dominate the picture. Another surface effect shown are the quasi head waves. These are generated along with the longitudinal wave, as this wave cannot satisfy the stress free boundary condition alone. In the isotropic case they propagate away from the surface with the speed of the transverse wave, see [3].

The calculation of each of these contour plots using the analytic solution has taken quite some time, between one and two hours on a PII-450 MHz. The Green's function may be considered to contain all the information there is to the wave problem, but it requires some effort to extract it through the numerical integration. Thus the approach is must suited when only information at some small domain is required, for example in

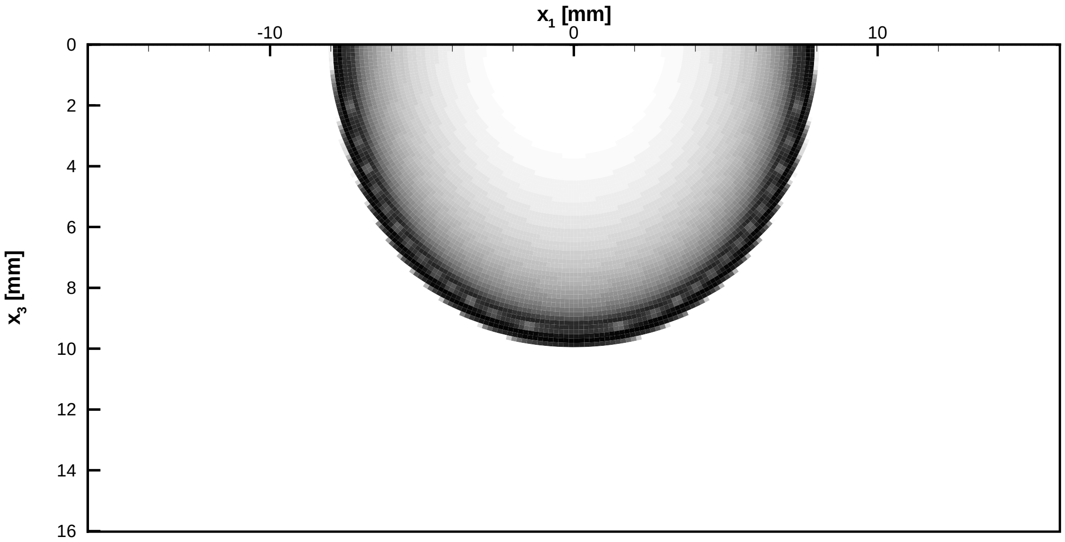

Figure 3.12: Contour plot from a SH point load, $\boldsymbol{q} = (0, 1, 0)$, situated at $(x_1, x_3) = (0, 0)$ for $t = 0.5\,\mu$s. Logarithmic plot included 35 levels with a range -45 dB to 0 dB (black).

connection with the calculation of an A-scan. The numerical approach to be studied in the next chapter requires the solution to be calculated at all points at successive points in time. Thus, we get the contour plots "for free". The above contour plots require only a few minutes to be calculated using the numerical approach. The more interesting contours are therefore postponed to the next chapter.

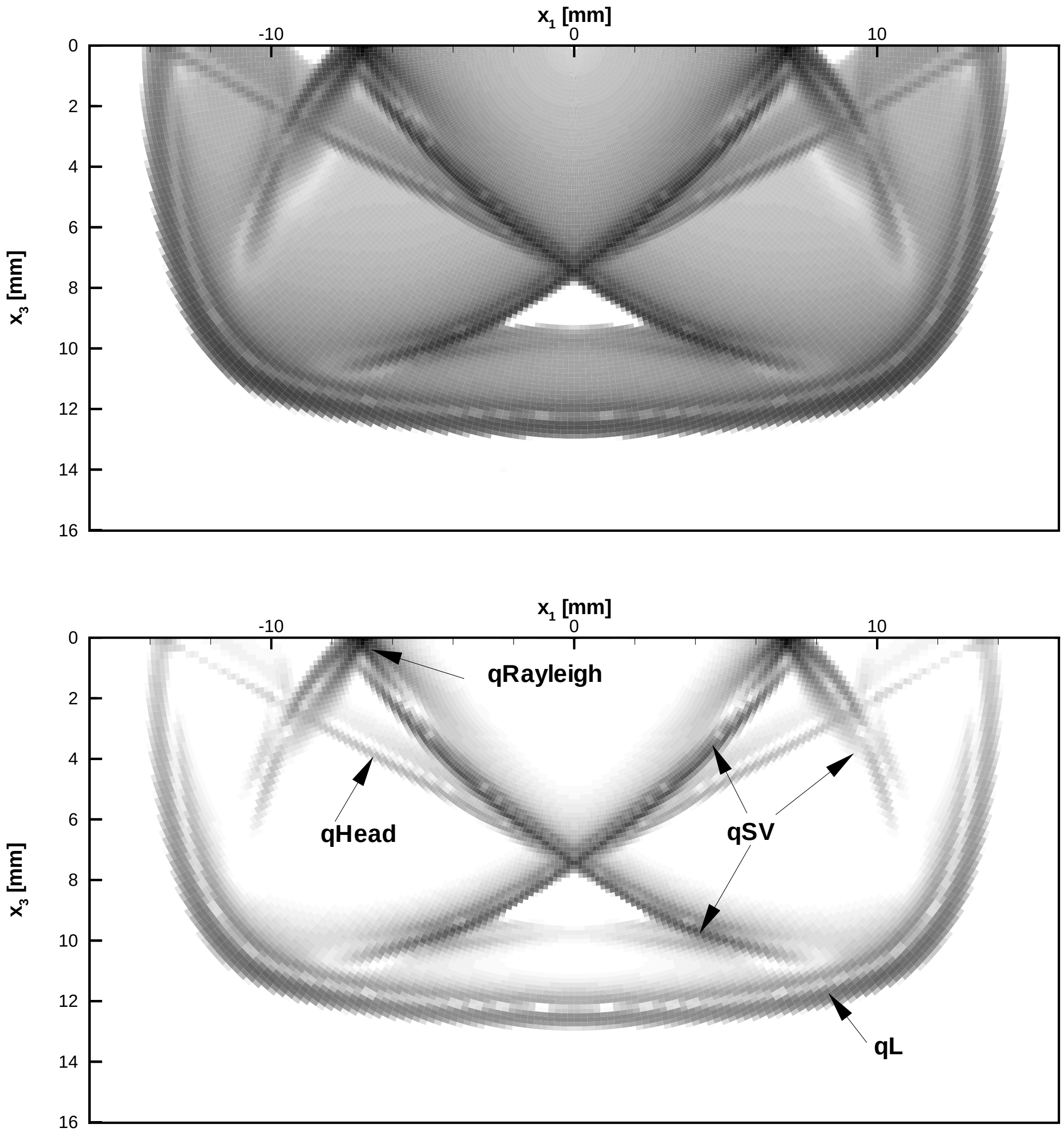

Figure 3.13: Contour plot showing the sound field from a point load situated at $(x_1, x_3) = (0, 0)$ and with direction of force $\boldsymbol{q} = (0, 0, 1)$ for $t = 0.5\,\mu$s. Upper logarithmic plot included 56 levels with range -72 dB to 0 dB (black) while the lower logarithmic plot included 35 levels with a range -45 dB to 0 dB (black).